



Deep learning of buckling instability in geometrically symmetry-breaking kirigami

Yunce Zhang ^{a,b}, Yafei Wang ^{c,d,*}, Qiang Tao ^e, Yuanpeng Liu ^{a,b,*}, Changguo Wang ^{a,b,**}

^a National Key Laboratory of Science and Technology on Advanced Composites in Special Environments, Harbin Institute of Technology, Harbin 150001, PR China

^b Center for Composite Materials and Structures, Harbin Institute of Technology, Harbin 150001, PR China

^c Department of Aeronautics and Astronautics, Fudan University, Shanghai 200433, PR China

^d Innovative Soft Material Engineering Lab, Department of Mechanical and Energy Engineering, Southern University of Science and Technology, Shenzhen, 518055, PR China

^e College of Mechanical and Electrical Engineering, Qingdao University, Qingdao 266071, PR China



ARTICLE INFO

Keywords:

Geometry-dependent kirigami
Buckling instability
Mechanics programmability
Symmetry breaking
Deep learning

ABSTRACT

Kirigami, subjected to escalating strain, frequently exhibits pronounced instability, coupled with remarkable flexibility and extraordinary extensibility. This behavior holds significant relevance for domains associated with malleable and reconfigurable surfaces, including stretchable electronics and modifiable functional devices. Nonetheless, conventional design methodologies, anchored in geometric symmetry and governed by minimum energy principles, tend to manifest buckling instabilities restricted to symmetric and anti-symmetric modes. To scrutinize the mechanisms of buckling behavior that disrupt geometric symmetry and comprehend the influence of geometry on programmability during reconfiguration, we propose an innovative strategy for kirigami's design. This strategy capitalizes on advanced deep learning methodologies, employing convolutional neural networks (CNNs) for categorizing buckling modes and recurrent neural networks (RNNs) for prognosticating constitutive relationships. Our approach furnishes a programmable design solution adept at identifying optimal kirigami patterns, characterized by their superior tensile strength and distinct buckling conformations, thereby fulfilling a diverse array of functional necessities. Our results illustrate that the proposed method displays a high level of precision in distinguishing between buckling modes of geometric symmetry and patterns that deviate from such symmetry. The buckling mode space has been extended and rediscovered, allowing unique modes to have the potential to be adopted into functional devices. Additionally, it demonstrates minimal losses in predicting constitutive relationships. Intriguingly, we discovered that tensile responses are geometry-centric and adjustable. Buckling modes showcase a dependency on geometry, with certain geometric parameters either significantly augmenting the sensitivity of buckling modalities or causing the buckling instability modes to become apathetic and unresponsive. Guided by the principle of target-led pattern parameter design, we proffer prospective tactics for the design of kirigami capable of delivering the desired mechanical performance. Moreover, we explore the feasibility of employing alternative biological materials in these designs.

1. Introduction

In recent years, the convergence of scientific and artistic disciplines, specifically kirigami and origami, has driven significant advancements in flexible and reconfigurable surface technologies. These developments have been primarily fueled by the underlying topological design principles of kirigami materials, which provide them with unique metamaterial-like characteristics. The remarkable metamorphic behavior exhibited by kirigami has resulted in its widespread application across various scales, including large-scale deployable space

satellite structures [1], programmable building skins [2], as well as microscale stretchable electronics [3–5], and nanocomposites [6]. However, designing kirigami structures systematically remains a persistent challenge, aiming to achieve diverse three-dimensional (3D) shapes through subtle modifications of the underlying geometric patterns in two-dimensional (2D) sheets. These methodologies enable the realization of a wide range of functionalities and mechanical properties. Such properties are often characterized by intricate transformations

* Corresponding authors.

** Corresponding author at: National Key Laboratory of Science and Technology on Advanced Composites in Special Environments, Harbin Institute of Technology, Harbin 150001, PR China.

E-mail addresses: wangyf@sustech.edu.cn (Y. Wang), liyp@hit.edu.cn (Y. Liu), wangcg@hit.edu.cn (C. Wang).

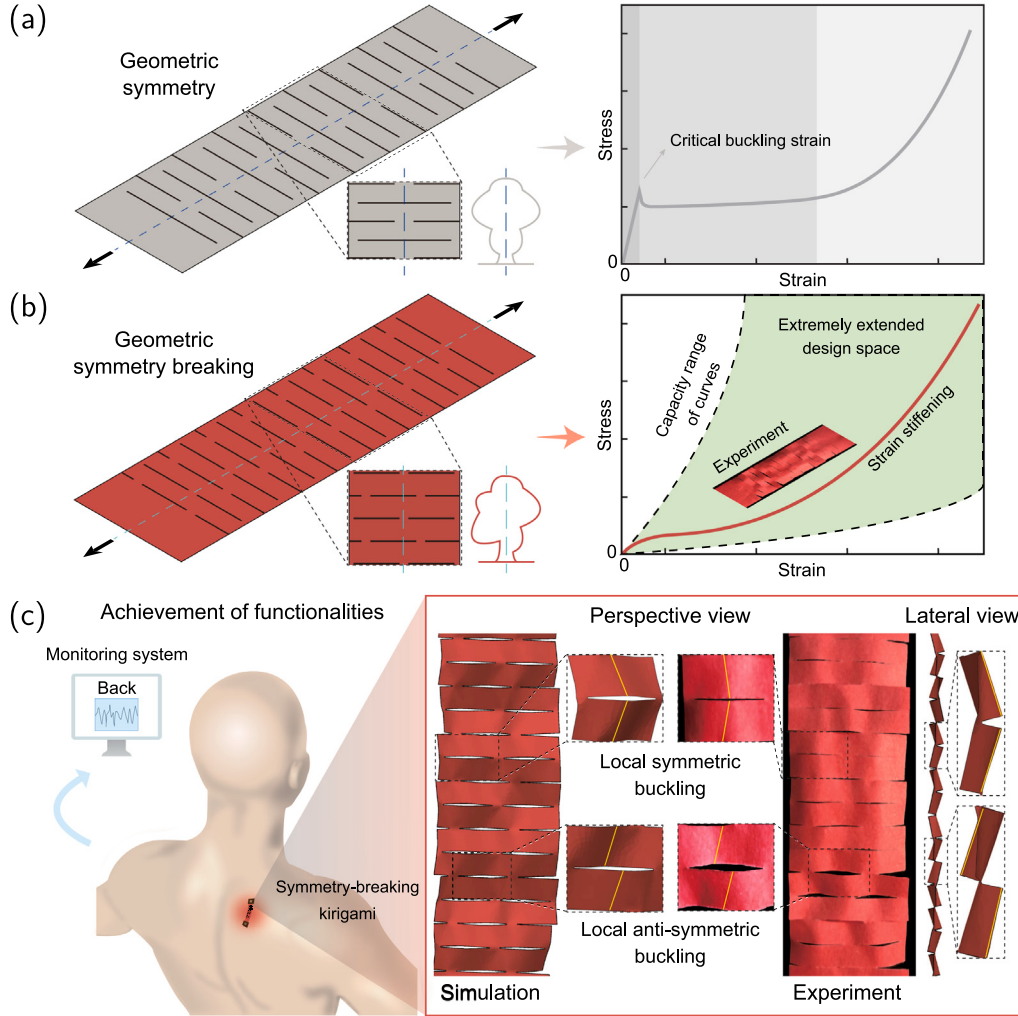


Fig. 1. Schematics of the initial and deformed configurations of kirigami structures. (a) The geometrically symmetric kirigami and its engineering elasticity. Its mechanical response can be described as three stages. When the tensile strain exceeds the critical buckling strain, the kirigami structure undergoes buckling. (b) The geometrically symmetry-breaking kirigami and its engineering elasticity. The geometric symmetry breaking can result in a variation of the mechanical response, which significantly extends design space and dramatically enhances capability of the stress-strain curve. (c) Local deformation mechanisms of kirigami structures. A variety of applications rely on their integration of local deformations. Two types of local deformation are identified by simulation and experimental observation. Kirigami with such deformation mechanisms can be used as a potential substrate material for sensors in flexible electronics.

of 2D sheets into complex 3D configurations, involving a combination of external morphological alterations and internal adjustments to the constitutive relationships. Strategically cutting patterns into thin sheets induces these variations, leading to multiple bifurcations and the breaking of geometric symmetries throughout the nonlinear process.

The first bifurcation point in kirigami structures, designed based on traditional symmetry principles, typically represents a critical threshold for the transition from in-plane to out-of-plane behavior. It is important to note that in ultra-thin two-dimensional materials, the primary physical mechanism often involves out-of-plane buckling, which prevails over in-plane deformation and crack propagation. For moderately thicker kirigami structures, the force-displacement curve displays three distinguishable progressive phases, with the presence of pre-buckling and predominantly in-plane rigid rotations, as illustrated in Fig. 1(a) [7]. The critical buckling strain serves as the boundary between the first and second phases. By carefully selecting appropriate geometric parameters and introducing a competition mechanism between symmetric and anti-symmetric modes, the occurrence of slightly complex deformation patterns after kirigami buckling can be triggered. The investigation of this buckling instability behavior in symmetric kirigami has been previously conducted using the theory of sinusoidal

beams [8]. An energy-based approach and principles from beam and plate theory have been employed to establish a theoretical framework for analyzing the tension-induced buckling of symmetric kirigami. This framework enables the determination of the flexibility and critical buckling strain of symmetric kirigami, thus validating its mechanical programmability.

Geometric symmetry breaking can blur this first bifurcation point, thus allowing the curve to be smooth [see Fig. 1(a-b) for details]. Geometric symmetry breaking, as an emerging design strategy, has exhibited remarkable potential in the field of kirigami. In contrast to traditional symmetric kirigami designs, the introduction of geometric symmetry breaking opens up an expansive design space, offering numerous novel possibilities [see Fig. 1(b) for details]. This exploration can be classified into two categories. The first category involves the introduction of additional boundary conditions by inserting small cuts at the tips of the original cuts, effectively enhancing the ultimate tensile strain [9]. The second category pertains to the utilization of inhomogeneous cutting patterns, which significantly mitigate undesired boundary effects [10]. It is noteworthy that both classes of cutting patterns induce buckling during stretching, exhibiting a similar nonlinear response observed in the aforementioned three progressive

phases [11]. The design of parallel cuts is more widely investigated and can be employed to alleviate stresses in elastic materials [12]. Subsequent improvements in its design can enhance buckling performance, stretchability, and flexibility [8,13]. However, kirigami structures are prone to plastic deformation and fracture damage at the cutting tips, limiting their ability to achieve high stretchability [14,15]. To address these undesired effects, finely-tuned cutting pattern designs have been developed, such as cuts with widened and rounded corners [16], reduced cut spacing [17], or hierarchical cuts [18]. The out-of-plane mechanism initially manifests as buckling, followed by instability in the post-buckling stage, resulting in lateral deformation of the structure at local weak points until a stable state is achieved. The emergence of this unique phenomenon in kirigami stems from the underlying kinematics of the cutting pattern, where externally applied tensile deformation in the global plane is counteracted by local compressive deformations in the planes adjacent to the cuts. Consequently, when the global tensile strain in kirigami surpasses a critical threshold, out-of-plane buckling occurs due to compression at the hinges near the cuts. Due to such unique characteristics, kirigami can be utilized as mechanically flexible and integrated devices for diagnostics and therapeutics in personalized healthcare. Kirigami accommodates the flexibility, comfort, adhesion, stretchability and shape programmability required for functional devices through two types of local buckling at the cutting position [see Fig. 1(c) for details] [19–23]. The elucidation of the relationship between geometric symmetry breaking cutting patterns and their corresponding mechanical responses remains unclear, necessitating further investigation.

Despite the significant progress made in developing reduced-order models [7,8,24,25] for symmetric and simple asymmetric kirigami designs, the field still lacks a comprehensive theoretical framework that accurately captures the explosive growth of buckling modes resulting from geometric symmetry breaking and the corresponding design space in kirigami. This raises a fundamental question: Can we establish a unified framework capable of accurately describing the explosive growth of buckling modes triggered by geometric symmetry breaking in kirigami, while enabling prospective design approaches that depart from the traditional “trial and error” paradigm [26]? We firmly believe that achieving this goal requires an active integration between geometry design and quantitative mechanical properties [27].

Deep learning techniques have emerged as a cutting-edge approach for analyzing and understanding complex relationships within various fields, including materials science and design. In the context of kirigami, these techniques hold great promise for advancing our understanding of the intricate connections between design patterns and their corresponding mechanical responses. By harnessing the power of large datasets, deep learning algorithms can effectively learn and recognize intricate patterns and correlations, enabling the identification of subtle associations between cutting patterns in kirigami and their resulting mechanical behaviors. This data-driven approach provides a unique opportunity to explore and unveil previously undiscovered insights into the underlying mechanisms governing the behavior of geometrically symmetry-breaking kirigami structures. The application of deep learning techniques in the realm of kirigami has already demonstrated its potential across different domains. For instance, in additive manufacturing, deep learning has been utilized to optimize processes and improve the quality and efficiency of fabrication [28–32]. In the field of metamaterials and metasurfaces, deep learning has played a crucial role in accelerating the design and discovery of novel structures with desired properties [33–43]. Moreover, in microstructure optimization, deep learning algorithms have been employed to enhance the performance and functionality of materials by tailoring their internal structures [44–46]. Additionally, deep learning has shown potential for more accurate predictions of material behavior under complex loading conditions, such as, modeling symmetry breaking and path-dependent plasticity [47,48]. Furthermore, in the realm of 2D kirigami nanomaterials, deep learning has facilitated the autonomous design and

discovery of new structures with tailored properties [49,50]. To the best of our knowledge, although there have been studies applying machine learning to kirigami, they only concentrate on fracture strain, yield strength and deformation of the unique kirigami structure [49–51], and do not involve the discussion of buckling modes and all-process mechanical responses, and this is the novel attempt for the solution of the target-led pattern parameter design problem of kirigami by utilizing the combined deep learning methods. By incorporating deep learning techniques into the study of kirigami, researchers can unlock a wealth of knowledge and insights, paving the way for more efficient design strategies, enhanced mechanical performance, and the exploration of novel applications. The ability to leverage vast amounts of data and extract valuable information from it empowers researchers to overcome the limitations of traditional design approaches, opening up new possibilities for the development of advanced kirigami structures with tailored functionalities.

In this paper, a unique deep learning-based design approach for kirigami is presented to acquire desirable cutting patterns and corresponding mechanical responses. Mechanical modeling of symmetric kirigami is illustrated to verify finite element (FE) simulation results with fabricated experimental samples. Then proposed deep learning approach is introduced to reach precise predictions for complex nonlinear constitutive relationships and buckling modes. Furthermore, multiple buckling modes including geometric symmetry patterns and geometric symmetry breaking patterns are divided to depict buckling morphologies and the effects on mode-dependence of different parameters are systematically examined. Moreover, the performance of our approach for four buckling examples is validated by experiments and simulations. Finally, alternative materials can be reverse designed to cover most of the biological materials Ashby plot with synthetic polymers in our approach. Through the target-led pattern parameter design, superior symmetry-breaking pattern candidates with multimodality are obtained to match various movement states and accommodate individual differences in health monitoring, which is not reached by geometrically symmetric kirigami. This study contributes mechanistic knowledge and predictive insights to address a symmetry-breaking challenge into kirigami design and its applications.

2. Symmetric kirigami and experimental benchmark

It is well known that the pristine two-dimensional planar structure is difficult to be stretched. When we conduct the cutting process on this planar structure, a kirigami is produced. In this case, the structure will be unstable in out-of-plane buckling when stretched, and thus has high stretchability. Kirigami considering buckling plays an outstanding role in applications such as flexible electronics, biodetection, and electrothermal devices [52–55]. In particular, its tensile property is a fundamental and essential mechanical property, which is directly related to reliability. This section outlines the tensile property of the symmetric kirigami and its experimental benchmark.

We start by performing mechanical tests to evaluate the tensile modulus and tensile strength. In these tests, kirigami structures can be fabricated from materials with low-elastic-modulus. Low-elastic-modulus can lead to deformation and instability buckling of this structure. Thus, experimental specimens are manufactured, whose material is made of high-density polyethylene (HDPE) with Young's modulus $E = 950$ MPa, Poisson's ratio $\nu = 0.38$, and thickness $t = 0.1$ mm. HDPE membranes with different geometrical parameters are tested together considering the comparison. Tensile tests are conducted using an electronic universal material testing machine (INSTRON-5965) and following the ASTM D882-02. Note that the magnitude of stretch (0.1 mm/s) is set, which ensures consistency of material deformation from the in-plane deformation to the out-of-plane deformation when the specimen is tested.

Next, the simulation results of the specimen have been verified by tests in our previous work [8]. Fig. 2 show stress-strain curves of two

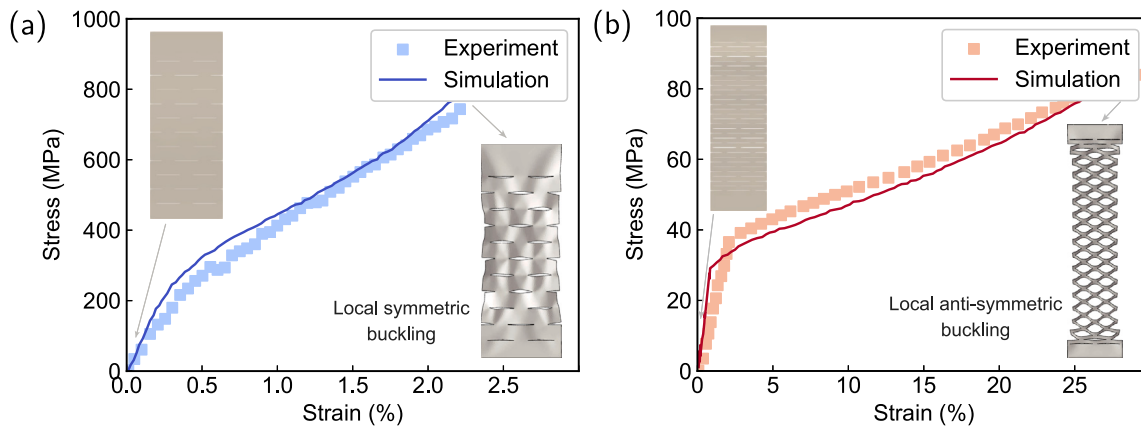


Fig. 2. Comparisons between experimental and simulation results of stress–strain curves for symmetric kirigami structures with different geometric patterns. Results indicate that various geometric patterns can contribute to distinct maximum tensile strains and overall buckling modes integrated by two local buckling, i.e., (a) local symmetric buckling and (b) local anti-symmetric buckling.

different specimens and prove that symmetric kirigami structures with different geometric parameters can produce various buckling deformations in uniaxial tension. The tensile performances of the kirigami structures are characterized by geometry-dependent effects. Then, buckling deformation results from the insets of Fig. 2 are given to reveal the morphological evolution of symmetric kirigami structures. The curves and the scatter points indicate the nonlinear stress–strain relationships as observed from simulations and experiments, respectively. The insets represent the postbuckling conditions of symmetric kirigami specimens in experiments and simulations at a late stage of tension. As the tensile displacement increases, the in-plane deformation gradually is converted to out-of-plane deformation, which subsequently stretches until complete fracture. The FE simulation results agree well with the experimental results. It should be noted that plastic deformation and fracture of symmetric kirigami are not involved here. This is because out-of-plane buckling is induced earlier than the appearance of cracks. The in-plane deformation of symmetric kirigami during the initial phase of stretching leads to the stress concentration and local tearing that should have occurred at the tip of the cut. But then that part of the energy is repaid by the out-of-plane deformation of symmetric kirigami. For the kirigami structure in Fig. 2(a), two neighboring slits are farther apart in the longitudinal direction, resulting in weaker interactions between the slits. In this case, a single slit generates a geometric incompatibility. The long distance between the slits allows only a small structural deformation of the kirigami structure, which is then load-bearing by the material, and there is a stress distribution on the whole surface of the kirigami structure after stretching, resulting in a low tensile strain and a high strength. For the kirigami structure in Fig. 2(b), the interaction between the slits increases as the spacing between the slits becomes smaller. Such a kirigami structure accomplishes the overall configuration change mainly through structural deformation. Under the tensile loading of the kirigami structure, the local deformation at the crack tip is repaid by the out-of-plane deformation of the kirigami structure, and the out-of-plane buckling is triggered much earlier than the stretching of the material. Therefore, only the tip of the slit has stress concentration phenomenon on the surface of this kirigami structure, while the sheet around the slit is basically stress-free. The stretching of the structure is completely borne by the structural deformation without stretching the material, so the tensile strain is high while the strength is low.

The undeformed geometry of the planar structure is defined by length L , width W and thickness t , completely. The undeformed geometry of kirigami is determined in the inset of Fig. 3. Besides the geometry, the mechanical response of kirigami is decided by its Young's modulus E , Poisson's ratio ν and uniaxial tensile displacement u . Geometric symmetry kirigami exhibits lateral buckling under uniaxial

tension, characterized by local symmetric and local anti-symmetric buckling. To understand the buckling behavior, a theoretical framework is proposed in Supplementary material. In general, kirigami structures undergo three stages in the stretching process as shown by the curve in Fig. 1(a): elastic stage, extension stage, and hardening stage. The geometrically symmetric kirigami structure in Fig. 2(b) shows mainly only the first two stages. The third hardening stage is very short. This is due to the small spacing of the slits, which makes the third stage not obvious according to the low threshold of material fracture. When symmetry breaking is introduced, as shown in Fig. 1(b), the geometrically asymmetric kirigami structure has its curved transition points blurred. Comparing with geometrically symmetric kirigami structures, the introduction of geometric symmetry breaking opens up a wide design space and provides many novel possibilities. This will be further discussed in the subsequent section.

3. Symmetry-breaking kirigami using deep learning

Taking advantage of the distinct characteristics of kirigami slits, we tap into their high designability. Through a combined approach of experiments and simulations, we can architect various symmetry-breaking kirigami patterns that control and foresee the mechanical performance and buckling behavior. The crux now lies in deploying kirigami to predict these properties reliably. This section outlines our deep learning (DL)-based methodology to build models and identify ideal kirigami structures for geometric patterns, as illustrated in Fig. 4.

3.1. Data generation for buckling kirigami

Building on our earlier experiments, it is highlighted that kirigami is fashioned from a membrane material as depicted in Fig. 1. In order to accurately represent the geometry-dependent traits, we have opted for kirigami with judiciously chosen dimensions; specifically, $W = 100$ mm and $L = 2(\ell_{sp} + \ell_{slit})$.

Through our experimental investigations, we have observed that different geometric patterns of kirigami structures exhibit varying mechanical properties and buckling modes. To validate these findings, we conducted finite element (FE) simulations on four representative kirigami choices and analyzed their stress–strain curves under uniaxial tensile loading, as depicted in Fig. 3. The stretchability of kirigami refers to the maximum strain that kirigami can achieve when the material is in its elastic stage. As shown in Fig. 3(c), the maximum strain point and deformation behavior of kirigami change with increasing strain, indicating the high sensitivity of stretchability and buckling modes to the topological configuration of the geometric pattern. It is evident that the relationship between the geometry and mechanical

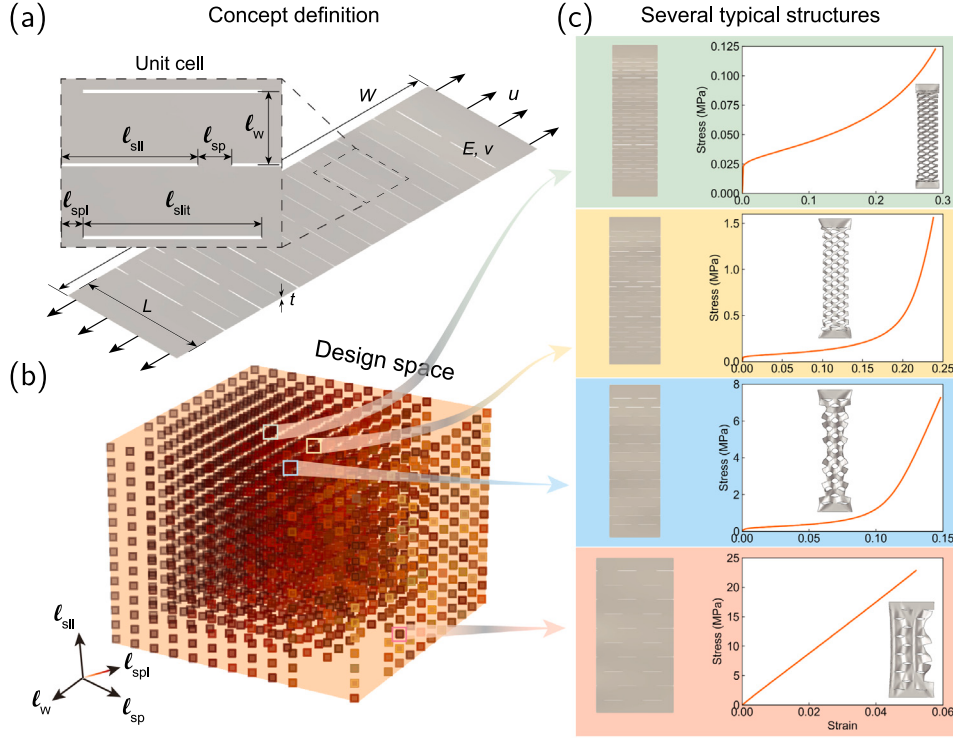


Fig. 3. Schematic diagram of the symmetry-breaking kirigami design. (a) The concept definition of kirigami showing details of the geometric parameters. (b) The design space and (c) representative kirigami structures of the precomputed pattern database. It provides the vast design space to kirigami optimization and candidate structures to achieve optimized tensile performances in flexible and functional applications.

properties of kirigami is complex and nonlinear. To describe the different geometric configurations, we introduce five geometric parameters in Fig. 3(a): ℓ_{slit} represents the slit length, ℓ_{sp} represents the spacing between two slits, ℓ_w represents the width between two slits, and ℓ_{sll} and ℓ_{spl} represent the distance of the slit and spacing from the left boundary in the unit cell, respectively.

By varying these geometric parameters, arbitrary kirigami patterns can be tuned and generated. However, the parameter design space for kirigami patterns is infinitely vast, making it impractical to explore through exhaustive experiments or simulations. Instead of traditional enumeration search methods, we propose employing deep learning (DL) models to search for desired symmetry-breaking kirigami patterns after training. For simplicity and representativeness, we impose constraints on these parameters during the training process. Considering manufacturing feasibility, we exclude parameter selections below a predefined minimum length scale of 1 mm. In this study, we set ℓ_{slit} as a constant value of 15 mm, and the remaining geometry constraints are presented as follows

$$\begin{aligned} \ell_w &\in \{3, 4, 5, 6, 7, 8, 9, 10, 11, 12, 15\}, \ell_{\text{sll}} \in \{1, 2, \dots, \ell_{\text{slit}}\}, \\ \ell_{\text{sp}} &\in \{3, 4, 5, 6, 7, 8, 9, 10, 11, 12, 15\}, \ell_{\text{spl}} \in \{1, 2, \dots, \ell_{\text{sp}}\}. \end{aligned} \quad (1)$$

To facilitate the selection process, we have constructed a substantial database comprising 14,850 unique kirigami samples, utilizing the aforementioned geometric parameters within the design space depicted in Fig. 3(b). This approach ensures the diversity of symmetry-breaking kirigami patterns while avoiding design duplications. While a larger parameter interval would result in a smaller database, which may suffice for specific kirigami designs, our objective is to provide a comprehensive range of properties and distinctive candidates that can be applied to various design scenarios. By employing this approach, the generation of the database is a one-time implementation, while the resulting database can be conveniently adapted to different design cases. As illustrated in Fig. 3(c), the constitutive relationships of kirigami structures within this precalculated database are solely

influenced by changes in geometric patterns, without any modifications to the constitutive materials.

In the DL model, the relationship between geometric patterns and displacement fields is established through data. Therefore, the preparation of representative data plays a crucial role in this design strategy. To accurately characterize and predict kirigami deformation, each unique kirigami configuration after stretching is paired with its corresponding stress-strain curve and buckling mode, as depicted in Fig. 4(a). The generated database encompasses two types of data: input data and output data. The input data primarily consists of geometric patterns and buckling modes, with geometric patterns described in detail by their geometric parameters, and buckling modes utilized for prediction and classification. The output data includes strain-stress curves and the classifications of buckling modes obtained from finite element (FE) simulations. The critical buckling strain, which determines the onset of buckling in symmetry-breaking kirigami, has been derived from analytical solutions in our previous work [8]. While the critical buckling mode governs the subsequent deformation path in the postbuckling regime, the entire postbuckling deformation process can only be characterized through numerical simulations. We have demonstrated that the critical buckling mode of kirigami, which minimizes strain energy, is highly sensitive to its geometric pattern [8]. Therefore, due to the geometric nonlinearity, numerical simulations using the commercial software ABAQUS are conducted in this study. The kirigami structure is an elastic material with a modulus of elasticity of 1000 MPa and a Poisson's ratio of 0.3. A static general step is used for the analysis. Vertical tensile displacements are applied to the upper and lower boundaries of the kirigami structure with a mesh size of 1 mm, using S4R cells and quad-dominated cell shapes. In addition, quasi-static conditions are ensured by monitoring the kinetic energy. To trigger instabilities, geometrical imperfections associated with modal superposition are introduced by calculating a linear perturbation analysis of the kirigami structure with the same geometry. To streamline the process, a Python code is developed to create a script that interacts with ABAQUS.

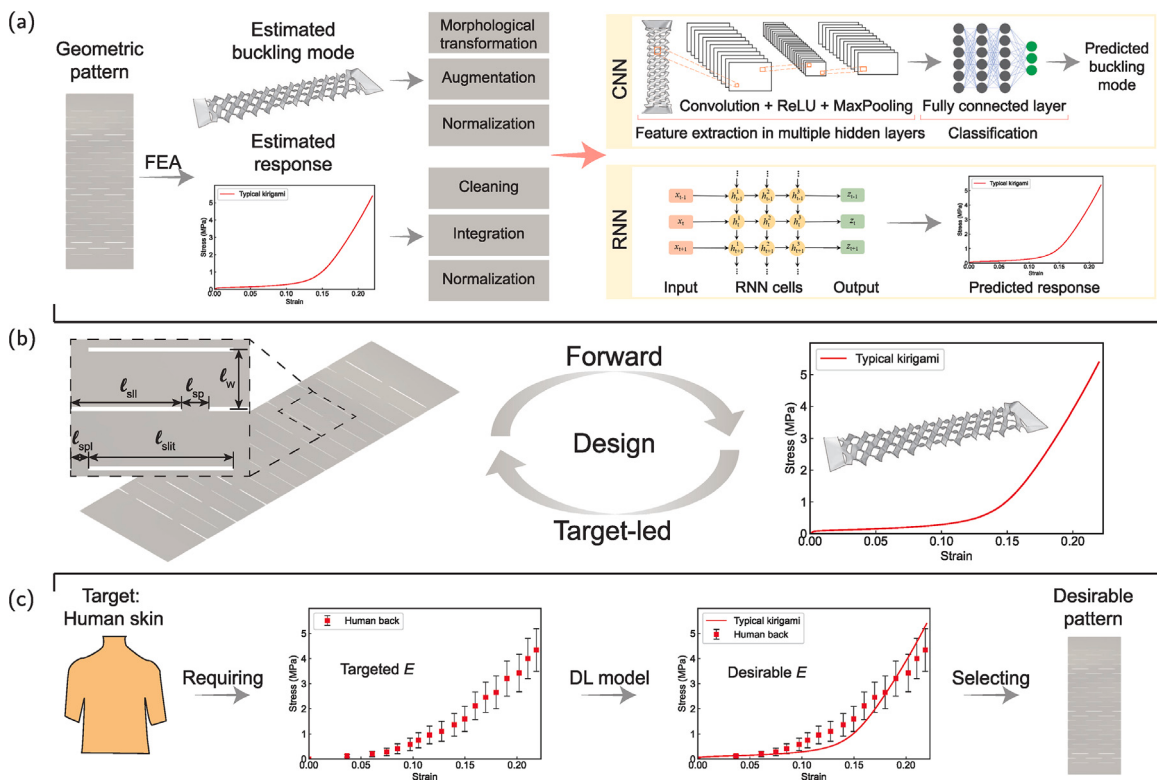


Fig. 4. Deep learning based framework for kirigami. (a) Dataset construction and data preprocessing which include the generation of kirigami structures, and their mechanical performances to establish the database. Forward learning based on the deep neural networks, which is employed to explore buckling modes and relation between stress and strain of kirigami structures. The insets show the architectures of defined deep neural networks. (b) Schematic descriptions of forward and target-led pattern parameter designs of kirigami in the framework of the kirigami design strategy. (c) Target-led pattern parameter design, which consists of a series of evolutionary steps to search for the ideal kirigami with the desired target functionality.

This script automates a series of operations including pre-processing, computation, and post-processing of kirigami numerical simulations using a general static solver. The script generates a geometric model by parsing the geometric descriptors of the varying kirigami structures. A reasonable mesh size is predefined and applied for meshing, followed by material assignment. Subsequently, boundary conditions and interactions are calculated, and a simulation file is created to perform the calculations. The final step of the script involves extracting and storing the numerical simulation output. Notably, this entire process is completely driven by the program without any human intervention.

3.2. Deep learning models for kirigami buckling prediction

This paper introduces two distinct types of deep learning models, as illustrated in Fig. 4(a). Kirigami structures undergo various buckling modes and exhibit complex post-buckling deformation relationships when subjected to stretching. The Convolutional Neural Network (CNN) is employed to predict and classify buckling mode images, while the Recurrent Neural Network (RNN) is utilized to forecast the intricate constitutive relations of kirigami structures. These models have demonstrated their efficacy in accurately predicting intricate mechanical material properties and deformation behaviors [48,56].

3.2.1. Convolution neural network

The Convolutional Neural Network (CNN) is an extension of multi-layer perceptron neural networks, specifically designed for processing image data represented as two-dimensional grids of pixels. This unique characteristic of CNNs has led to significant advancements in tasks such as self-driving cars [57] and face recognition [58]. CNNs excel at predicting and classifying image data due to their ability to capture spatial relationships effectively. Furthermore, the parallelizability of

convolution operations across GPU cores enables CNNs to be computationally efficient and capable of generating accurate models with minimal data samples. In this study, we leverage a CNN-based neural network to train our computational buckling images using labeled buckling modes, as shown in Fig. 5. The database generated from mechanical simulations is divided into input vectors, denoted as \mathbf{X} , and output vectors, denoted as \mathbf{Y} . In the neural network framework, the inherent structural information present in the images is abstracted and represented as numerical vectors in the input vector \mathbf{X} . The output vector \mathbf{Y} encompasses the various buckling modes observed in kirigami structures. Then the input and output vectors are expressed in the functional form

$$\mathbf{X}_{i,j} = \hat{\mathbf{X}} [X_{11}, X_{12}, \dots, X_{1j}; X_{21}, X_{22}, \dots, X_{2j}; \dots; X_{i1}, X_{i2}, \dots, X_{ij}], \text{ and} \\ \mathbf{Y} = \hat{\mathbf{Y}} (Y_1, Y_2, \dots, Y_n), \quad (2)$$

where $\mathbf{X}_{i,j}$ denotes numerical values corresponding to the pixels of the image data, i.e., the pixel at location (i, j) in the input image. \mathbf{Y} is the classifications of the image data. As discussed above, an CNN can be defined as a mapping form

$$\mathbf{Y} = \hat{f}_{\text{CNN}}(\mathbf{X}_{i,j}). \quad (3)$$

Similar to the general neural network, the CNN is divided into an input layer, the hidden layers and an output layer. The hidden state vector $\mathbf{H}_{i,j}$ can be calculated to indicate the pixel at location (i, j) in the immediate hidden representation. Thus the hidden matrix $\mathbf{H}_{i,j}$ can be given by the fully connected layer as a functional form [59]

$$\mathbf{H}_{i,j} = \sum_k \sum_l W_{i,j,k,l} \mathbf{X}_{k,l} + \mathbf{B}_{i,j} = \sum_a \sum_b V_{i,j,a,b} \mathbf{X}_{i+a,j+b} + \mathbf{B}_{i,j}, \quad (4)$$

where \mathbf{W} and \mathbf{B} represent the weight matrices as fourth-order tensors and the biases, respectively. Then $V_{i,j,a,b} = W_{i,j,i+a,j+b}$ is set. The indices

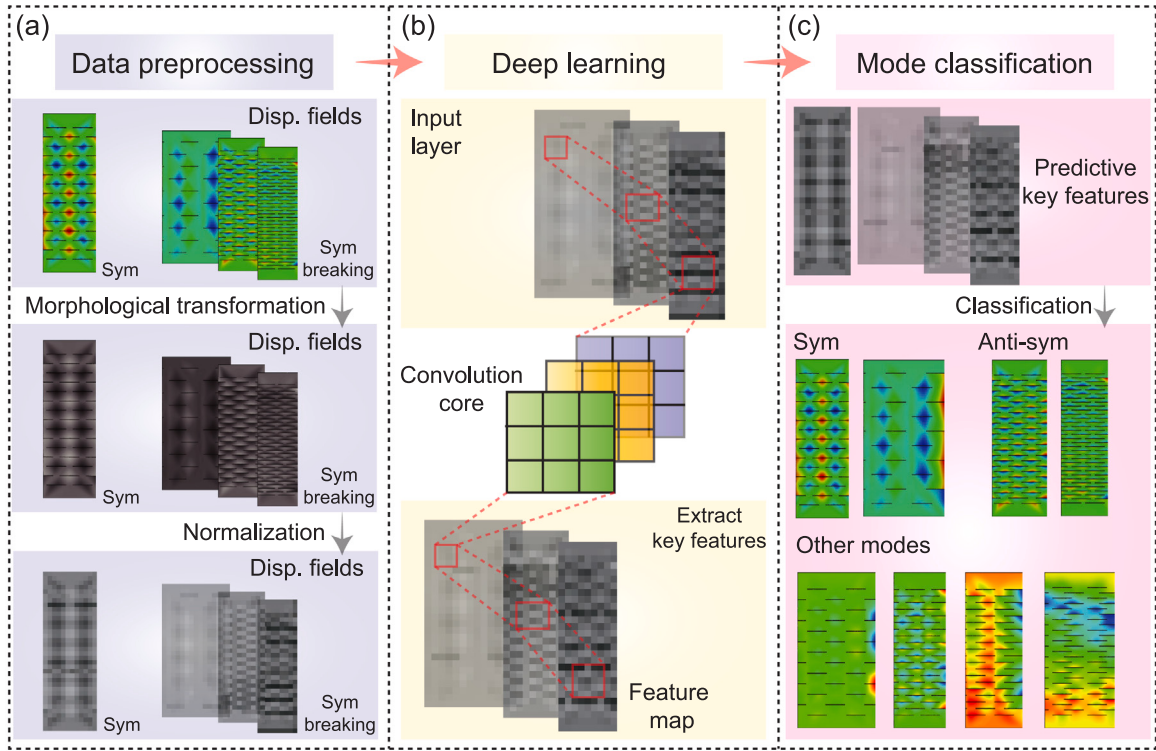


Fig. 5. Workflow of deep learning in displacement fields for the inverse identification of kirigami buckling modes. (a) Data preprocessing. The displacement fields are transformed for better identification and the key features are conserved in the next CNN model. (b) CNN model in the displacement field as the input layer and its extracted key features as feature maps, respectively. (c) Mode classification. The predicted key features in displacement fields of kirigami structures by CNN model are classified to obtain the different buckling modes.

a and b cover the entire image, running across both positive and negative offsets. However, this requires the large number of parameters, beyond what computers can address. Next, two operations, translation invariance and locality, are performed to obtain the convolutional layer

$$\mathbf{H}_{i,j} = \sum_a \sum_b \mathbf{V}_{a,b} \mathbf{X}_{i+a,j+b} + b_0, \text{ and } \mathbf{H}_{i,j} = \sum_{a=-\Delta}^{\Delta} \sum_{b=-\Delta}^{\Delta} \mathbf{V}_{a,b} \mathbf{X}_{i+a,j+b} + b_0, \quad (5)$$

where $\mathbf{V}_{a,b} = \mathbf{V}_{i,j,a,b}$ is a convolutional kernel and $\mathbf{B}_{i,j}$ is a constant, described b_0 . To extend this, different features embedded in the image are extracted using multiple kernels of the same dimensionality. Therefore, the output of the convolution layer will be a feature mapping of the results of multiplying different kernels with the input image as shown in Fig. 5(b).

3.2.2. Recurrent neural network and gated recurrent unit

The Recurrent Neural Network (RNN) extends the capabilities of feed-forward neural networks and is particularly well-suited for handling input vectors of varying lengths. RNNs excel in tasks involving sequential data, such as natural language processing and speech recognition [60]. By utilizing hidden states that retain information from previous inputs, RNNs can effectively incorporate historical data to make predictions for future outputs. In the context of this study, stress-strain curves are employed as both the training input and output data in the deep learning approach. This choice enables the integration of prior knowledge regarding the mechanical response of kirigami structures from experimental observations and simulations, facilitating a more accurate characterization of the deformation behavior. The stress response of kirigami can be defined by

$$S = \mathcal{F}/A, \quad (6)$$

where \mathcal{F} represents the vertical tensile force of kirigami and A is the cross-sectional area of kirigami. The integration of the prior knowledge obtained from experiments and simulations into the neural network via the stress-strain curves will effectively increase the learning concentration and improve its accuracy.

The generated database acquired from the mechanical simulations is split into input vectors and output vectors, indicated as X and Y , respectively. In the neural networks, the input vector X is assumed to rely on the geometric patterns and the strain array, $\varepsilon_1, \varepsilon_2, \dots, \varepsilon_n$. The output vector Y is only considered to include the global stress of kirigami, S , as shown in Fig. 6(a). This functional form can be described as

$$X = \hat{X}(\ell_w, \ell_{sp}, \ell_{sll}, \ell_{spl}, \varepsilon_1, \varepsilon_2, \dots, \varepsilon_n), \text{ and } Y = \hat{Y}(S_1, S_2, \dots, S_n), \quad (7)$$

where ε_n and S_n denote values of strain and stress at the current time t_n . Considering the history-dependent behavior of constitutive relationships, information on the history of ε and S is prescribed. As discussed above, an RNN can be defined as a mapping form

$$Y_N = \hat{f}_{RNN}(X_1, X_2, \dots, X_N), \quad (8)$$

where $X_n = X(t=t_n) \in \mathbb{R}^{n \times d}$ (number of examples: n , number of inputs: d), for $1, 2, \dots, N$, represent N time-dependent input vectors and $Y_n = Y(t=t_n) \in \mathbb{R}^l$ (number of examples: l) represents the mapped output vector at time step $t=t_n$.

Due to the issue of vanishing or exploding gradients, capturing long-term dependencies in Recurrent Neural Networks (RNNs) has been challenging [61]. However, this problem has been addressed with the introduction of Long Short-Term Memory (LSTM) networks [62]. In a similar vein, the Gated Recurrent Unit (GRU) has emerged as another solution to tackle this challenge. GRU incorporates adaptive “reset” and “update” memory units, replacing the input gate and forget gate of LSTM with the update gate and reset gate, respectively, which are calculated at the current time step. While LSTM and GRU demonstrate

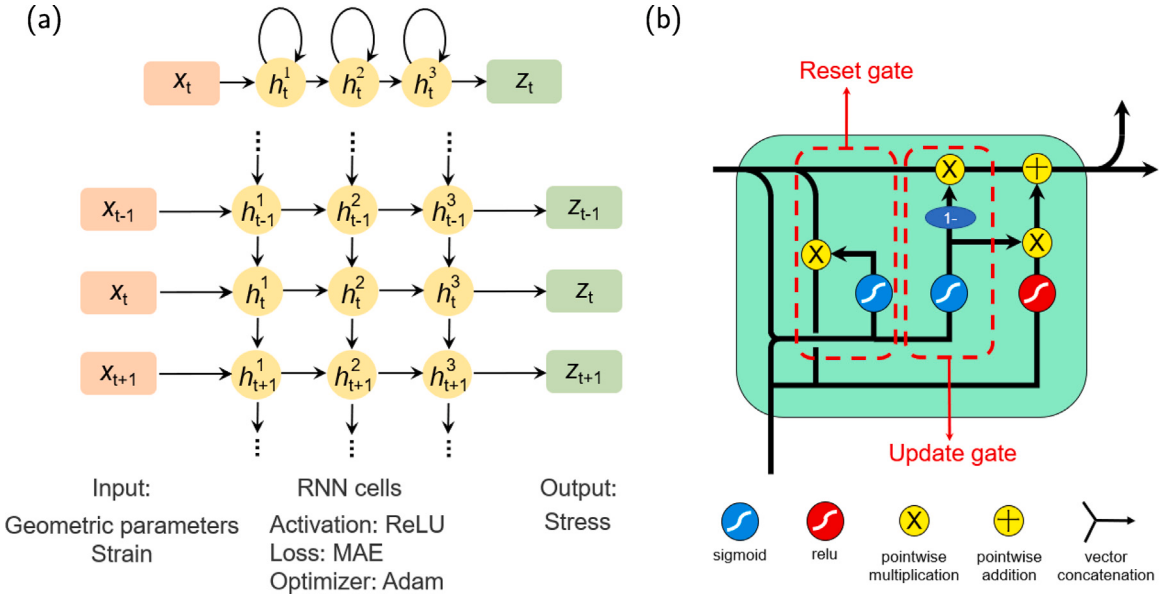


Fig. 6. (a) The main building blocks of recurrent neural network (RNN). (b) Operations of the GRU unit to update the hidden layer at time t according to the input at time t and the hidden state at time $t - 1$. RNNs can be defined as a mapping form through main building blocks and GRU units.

comparable computational abilities in various tasks [63], GRU exhibits the ability to balance the previous and current hidden states and reveal the memory content, as illustrated in Fig. 6(b). Additionally, GRU has a smaller number of variables compared to LSTM, which aids in convergence. In the GRU model, the reset gate and update gate are first computed.

The specific equations correspond to the first hidden layer can be provided in Supplementary material. Subsequent hidden layers can be expressed as

$$\begin{aligned} \mathbf{R}_n^i &= \phi \left(\mathbf{W}_{XR}^i \mathbf{X}_n + \widetilde{\mathbf{W}}_{HR}^i \mathbf{H}_{n-1}^i + \mathbf{b}_R^i \right), \\ \mathbf{U}_n^i &= \phi \left(\mathbf{W}_{XU}^i \mathbf{X}_n + \widetilde{\mathbf{W}}_{HU}^i \mathbf{H}_{n-1}^i + \mathbf{b}_U^i \right), \\ \tilde{\mathbf{H}}_n^i &= \tanh \left(\mathbf{W}_{XH}^i \mathbf{X}_n + \widetilde{\mathbf{W}}_H^i (\mathbf{R}_n^i \odot \mathbf{H}_{n-1}^i) + \mathbf{b}_H^i \right), \\ \mathbf{H}_n^i &= \mathbf{U}_n^i \odot \mathbf{H}_{n-1}^i + (1 - \mathbf{U}_n^i) \odot \tilde{\mathbf{H}}_n^i, \quad \text{with } i = 2, 3, \dots, M. \end{aligned} \quad (9)$$

The above equations are performed iteratively until the state of the last hidden layer state vector \$\mathbf{H}_N^M\$ at time \$t = t_N\$ is achieved. In this manner, the final output vector

$$\mathbf{Y}_N = \mathbf{W}^O \mathbf{H}_N^M + \mathbf{b}^O, \quad (10)$$

where \$\mathbf{W}^O \in \mathbb{R}^{l \times h^M}\$ and \$\mathbf{b}^O \in \mathbb{R}^l\$ represent the weight matrix and the bias of the output layer, respectively.

3.3. Refinement of hyperparameters and architecture optimization

In this study, the Keras library [64] is employed to construct the CNN and RNN models. For the CNN model, convolutional feature maps are combined with hidden layers, followed by a dense layer to classify post-buckling kirigami images into 8 categories. In the RNN model, RNN cells are used in conjunction with multiple hidden layers and a time-distributed dense layer [64] to transform the two-dimensional outputs of the RNN cells into the desired output, which corresponds to the stress-strain curves of kirigami during deformation increments. The GRU architecture is selected due to its superior accuracy compared to other RNN architectures [48]. To optimize the performance of the models, hyperparameter analysis is conducted to determine the appropriate number and size of hidden layers. Further details regarding this analysis are provided in the subsequent discussion. To evaluate the accuracy of predictions, the mean squared error (MSE) is utilized as the

error metric. The mean absolute error (MAE) is employed as the loss function, which quantifies the disparity between predicted values and actual values MSE can be obtained as

$$\text{MSE} = \frac{1}{n_s} \sum_{i=1}^{n_s} (\hat{Y}_i - f(\bar{X}_i))^2, \quad (11)$$

where \$n_s\$ is the number of samples and \$\hat{Y}_i\$ and \$f(\bar{X}_i)\$ represent the \$i\$th target value and the prediction of a neural network, respectively.

Meanwhile, by reasonably computing the gradient of the loss function for each epoch and then iterating over the parameters, the Adam optimizer [64] is employed in this work. For hidden layers, two activation functions including sigmoid \$S(x)\$ [65] and Rectified Linear Unit (ReLU) \$R(x)\$ [66] are selected with the expression as

$$S(x) = \frac{1}{1 + e^{-x}}, \text{ and } R(x) = \max(0, x). \quad (12)$$

During the data preprocessing stage, it is essential to normalize the input data (i.e., kirigami descriptors and deformation paths) as well as the output data (i.e., stress and buckling modes) from the database to the range [0, 1]. This normalization process promotes model training and enhances accuracy. Based on the aforementioned processes, we construct and train the deep learning (DL) models, as depicted in Fig. 4(a), to establish a clear correlation between geometric parameters and mechanical performance in the database.

The datasets used for training and validation in the DL models, namely the training set and validation set, account for 80% and 10% of the database, respectively, while the remaining portion is allocated for the test set. As illustrated in Fig. 4(a), finite element (FE) simulations of kirigami structures are conducted, followed by the implementation of DL models to predict their stretching performance. The loss function employed in the training process aims to quantify the discrepancy between the DL model predictions and the FE simulation results. Through iterations, the loss function is computed and gradually reduced, indicating the convergence and consistency between the two methods, thereby validating the trained model. As the iterations progress, the predicted stress-strain curve will closely match the data from the test set. The complexity of DL models can lead to a decrease in the computational loss value within the training set as the number of units or layers in the model reasonably increases. This appropriate complexity ensures accuracy in the model without encountering issues such as overfitting or underfitting. To illustrate the workflow of forward and

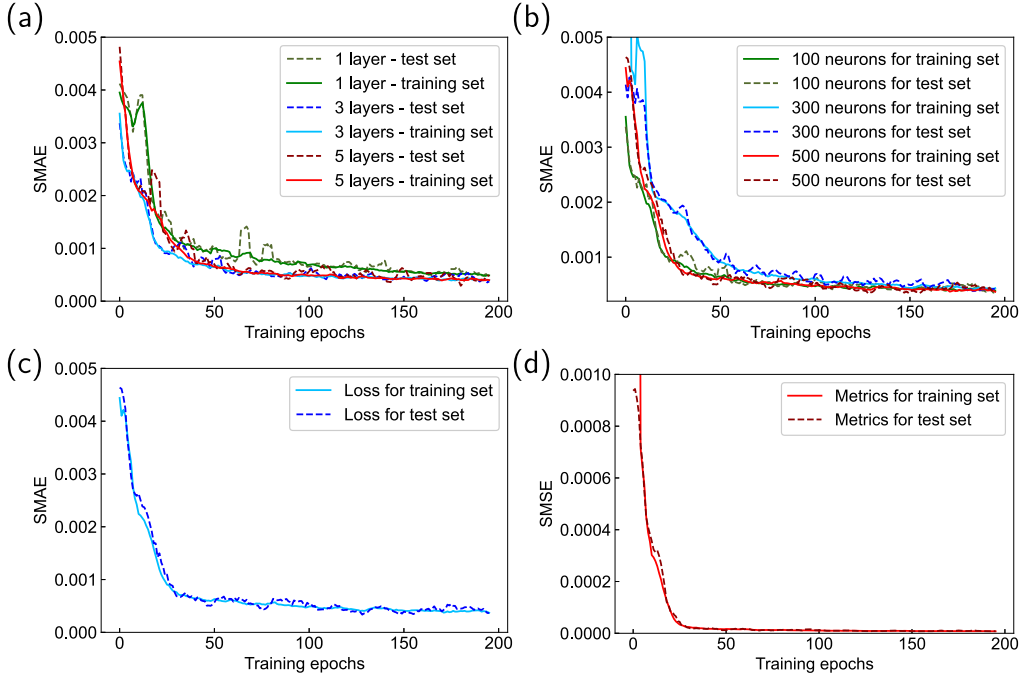


Fig. 7. The hyperparameter analysis results and the predictive performance of the selected RNN model. (a) Hyperparameter analysis of the RNN model for the number of stacked GRU layers and (b) the number of neurons in GRU cells. (c) The loss and (d) the metrics for the training set and the test set. Based on the analysis of hyperparameters and configurations, the optimal setup for the RNN model involves 3 GRU layers and 500 neurons to achieve the best results. After 200 epochs of iteration, the prediction losses and metrics values for the training and test sets are sufficiently low.

target-led pattern parameter designs, a specific geometric pattern of kirigami is presented in Fig. 4(b). Additionally, Fig. 4(c) showcases the evolutionary steps involved in designing and selecting an ideal kirigami pattern, which will be further discussed in subsequent sections with more details.

4. Buckling instability results in symmetry-breaking kirigami

As described earlier, a total of 14,850 geometric patterns for kirigami structures were generated and subjected to finite element (FE) simulations to characterize their tensile performance. This section outlines the performance of DL models based on simulations and buckling instability and nonlinear results in symmetry-breaking kirigami.

4.1. Performance of DL models

In the simulations, the kirigami models were incrementally stretched, starting with a pre-buckling stage exhibiting in-plane deformation, followed by a post-buckling stage with out-of-plane deformation until the displacement exceeded the critical buckling threshold. Finally, the structures were stretched until fracture. The computational complexity of the tensile process resulted in an average wall time of 4 min per simulation on a Ryzen 9 12-core processor. Mathematically, the geometric designs of symmetry-breaking kirigami can be infinitely varied by controlling the four geometric parameters. To strike a balance between including representative models and reducing the workload of FE simulations, geometric constraints were introduced. From Fig. 3(a), it can be observed that $\ell_{\text{slit}}/\ell_w, \ell_{\text{slit}}/\ell_{\text{sp}} \in [1, 5]$ and $\ell_{\text{slit}}/\ell_{\text{sll}}, \ell_{\text{slit}}/\ell_{\text{spl}} \in [1, 15]$ were specified as the geometric constraints, forming a vast design space as shown in Fig. 3(b).

In this study, the architecture selected for the GRU formulation involves a second-level hidden state. This choice allows the GRU units to directly access the hidden state of history-dependent, temporal inputs, and non-temporal inputs, thereby improving accuracy compared to other RNN architectures [48]. Two activation functions, sigmoid and ReLU, are utilized, and the mean absolute error is employed as

the loss function. The Adam optimizer with a tuned learning rate is used, and the model is trained for 200 epochs. It is worth noting that the DL model can provide much faster predictions compared to FE simulations. For instance, the generated DL model predicts the mechanical performance of kirigami in 41 ms on a NVIDIA GeForce RTX 2070, while it takes nearly 4 min to perform an FE simulation on a Ryzen 9 12-core processor. Although the actual computing time may vary depending on the hardware, it is evident that this data-driven approach enables faster prediction and evaluation. The use of RNN models to generate tensile performance for kirigami structures with diverse geometric patterns, rather than relying solely on intricate FE simulations, is significant for geometric optimization.

The hyperparameters and configurations of the developed DL models are optimized, considering aspects such as dropout layers, normalization processes, and optimization algorithms. Fig. 7(a) presents the results obtained from different stacked GRU layers, evaluated using the scaled mean absolute error (SMAE). The findings indicate that a single GRU layer is insufficient to support the necessary computational complexity of the model. Furthermore, the predictive capability of the model with 5 GRU layers is similar to that of the model with 3 GRU layers, but the former requires more training time and computational resources. Therefore, RNN models with 3 GRU layers are employed in this work. Similarly, Fig. 7(b) shows that the model with 500 neurons performs relatively optimally compared to models with 100 and 1000 neurons. Therefore, based on the analysis of hyperparameters and configurations, the optimal setup for the RNN model involves 3 GRU layers and 500 neurons to achieve the best results. Fig. 7(c-d) demonstrate the predictive evaluations of the training and test sets, focusing on the loss and metrics of the RNN model. After 200 epochs of iteration, the prediction losses for the training and test sets are sufficiently low at 0.00048503 and 0.00051059, respectively, with low metrics values of 0.000014289 and 0.000014586 for both sets. The configuration and evaluation of the CNN model will be discussed in Section 4.2.

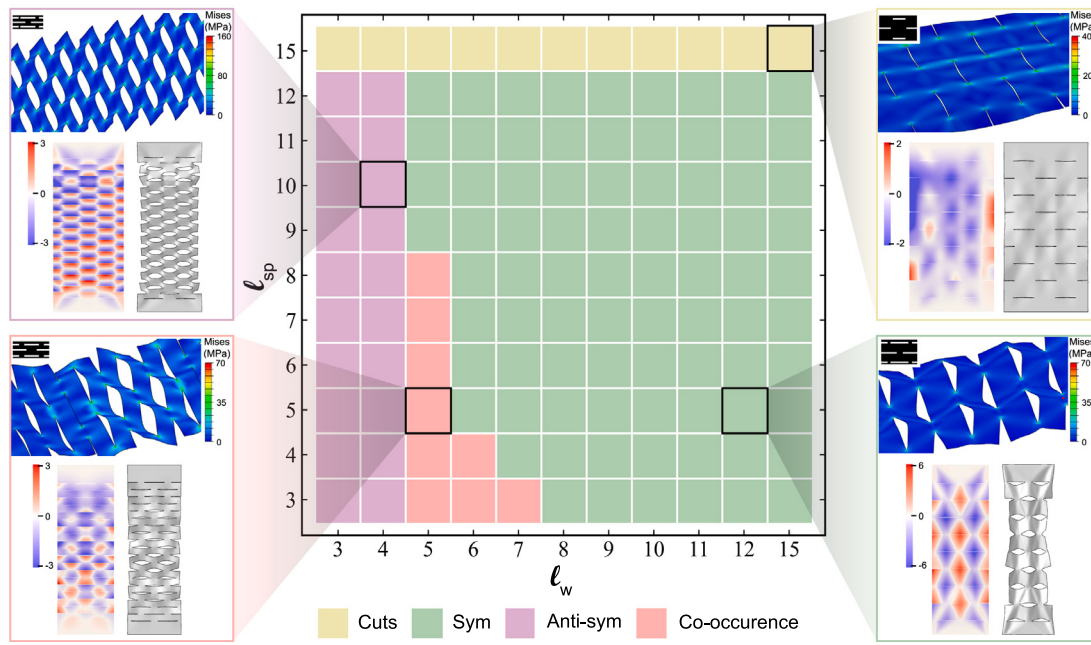


Fig. 8. The symmetric kirigami images and results. Buckling images of four typical configurations using FE simulations showing the out-of-plane deformation. Unit of the color bar is in mm. Phase diagram demonstrating the variations in buckling configurations of kirigami structures, as the values of ℓ_w and ℓ_{sp} are varied and four typical modes showing different buckling configurations.

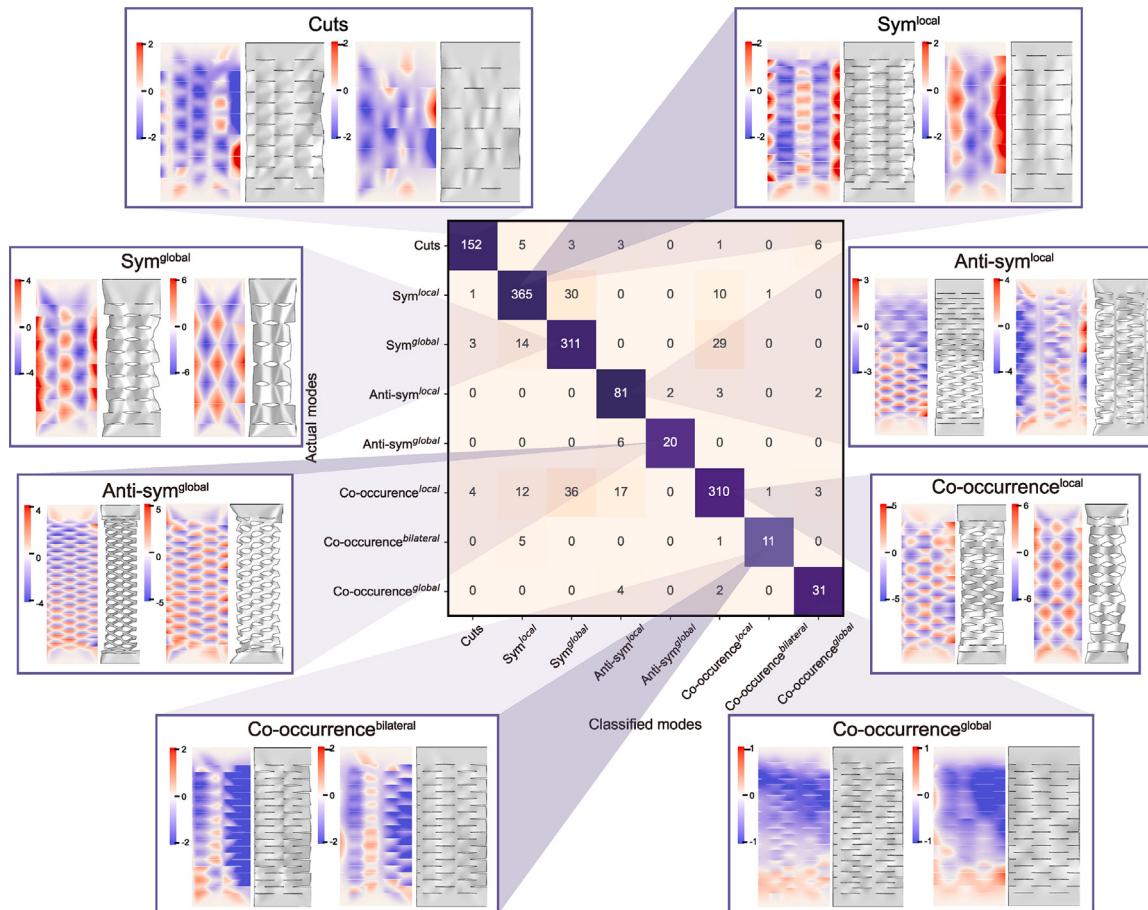


Fig. 9. Kirigami images and results in the CNN model. Confusion matrix of eight typical modes with buckling images of typical configurations using FE simulations showing the out-of-plane deformations. Unit of the color bar is in mm. The CNN model identifies and classifies the different buckling modes with a good classification accuracy.

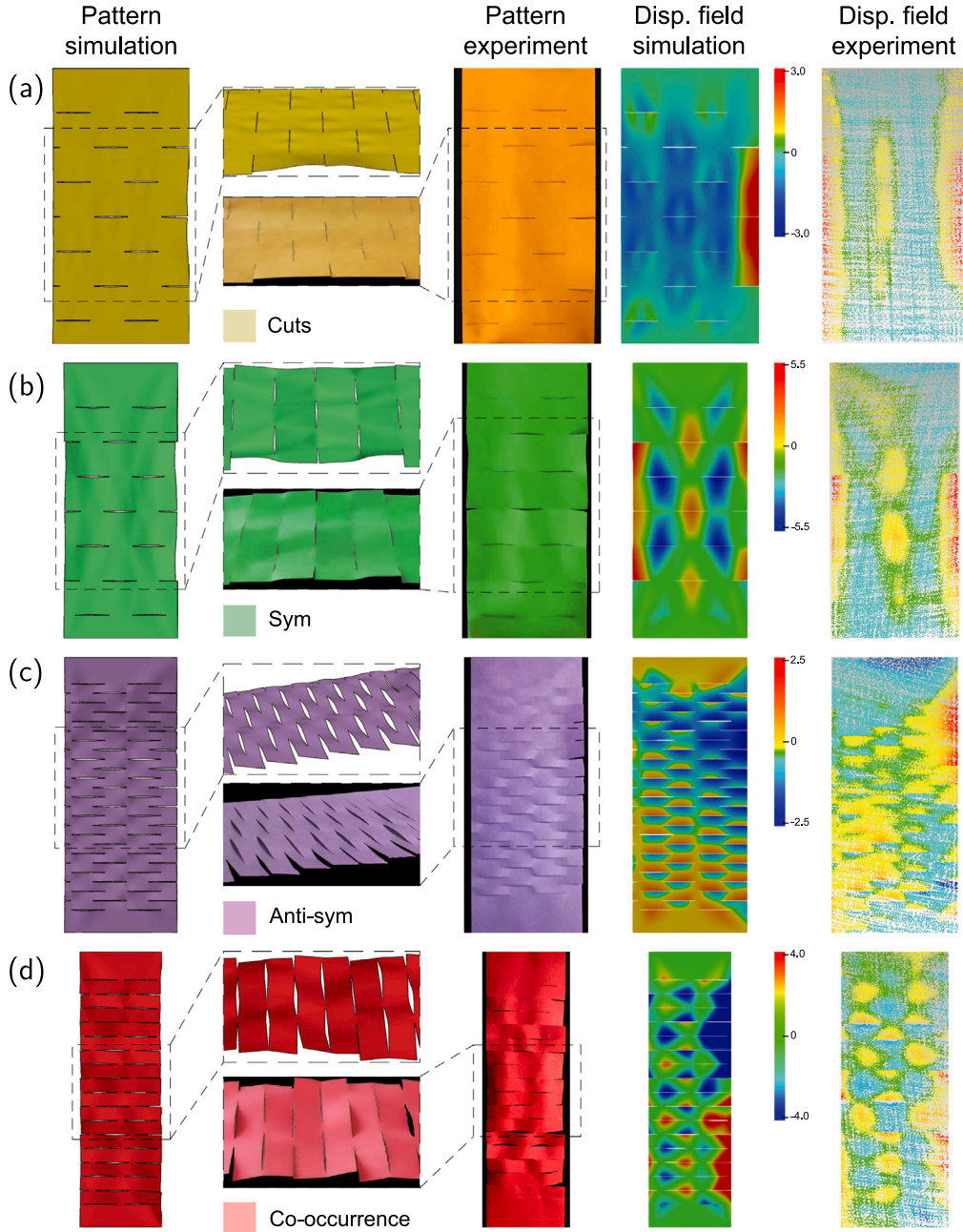


Fig. 10. The performance of our method on four buckling modes with numerical and experimental validations. (a) Cuts. (b) Sym. (c) Anti-sym. (d) Co-occurrence. The results from simulations and experiments show that the method in this study can predict the buckling modes of kirigami structures well in terms of geometric patterns and displacement fields. The displacement field experiments are tested by a T-Cam MR digital camera system.

4.2. Explosive multistable buckling mode space and verifying nonlinear behavior

For kirigami with geometrically symmetric patterns, a series of systematic studies have been conducted to investigate their mechanical behavior under uniaxial tension by varying ℓ_{sp} and ℓ_w within reasonable ranges, as discussed in our previous work [8]. Fig. 8 presents four buckling modes that illustrate the post-buckling state of kirigami during the later stages of stretching, along with a phase diagram depicting these modes. The ‘Cuts’ mode is observed when $\ell_{sp} = \ell_{slit}$. In this case, the spacing between adjacent slits in the vertical direction is large, leading to minimal interaction between the slits in accordance with St. Venant’s principle. Consequently, due to the geometrical incompatibility of individual slits, only a slight degree of out-of-plane

buckling occurs around the slits. Thus, this buckling mode is primarily influenced by in-plane stretching.

With a decrease in ℓ_{sp} , thin kirigami structures undergo lateral buckling, leading to the development of three additional buckling modes. As the interaction between the slits intensifies, the buckling configuration of kirigami gradually transitions into a system dominated by out-of-plane bending. Changes in other geometric parameters result in different types of local buckling, namely local symmetric buckling and local anti-symmetric buckling. Local symmetric buckling is characterized by out-of-plane displacement symmetric about the transverse axis of symmetry, while local anti-symmetric buckling is the opposite. These two types of local buckling represent local energy minimum points in kirigami buckling. Integrating these local buckling results in three other buckling modes: mode Sym, mode Anti-sym, and mode Co-occurrence. Mode Sym and mode Anti-sym indicate the prevalence of

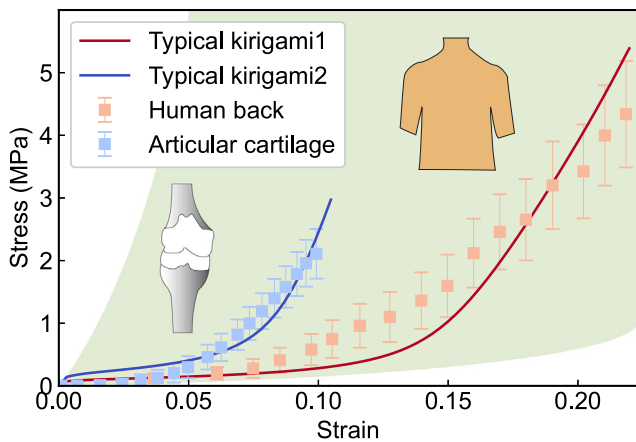


Fig. 11. Bio-mimetic applications for stress-strain responses in the human back skin [67] and the articular cartilage [68], along with the results of typical kirigami designs. Here, the green region indicates the capacity of the stress-strain curve that kirigami can achieve. Any required stress-strain curve in this region can be reverse designed by our method to search for a corresponding well-matched kirigami candidate.

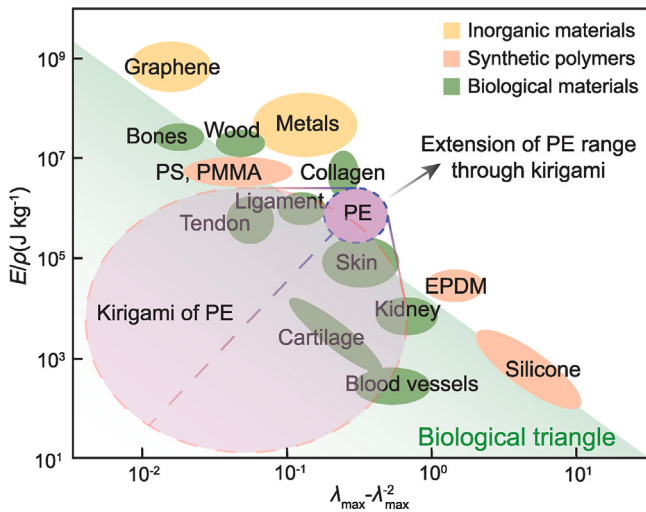


Fig. 12. A broad range of Young's moduli for most materials at a wide range of elongation-at-break plotted on an Ashby diagram [69]. Most biological materials can fit the biological triangle rule, demonstrating a reasonably low Young's moduli at moderate stretchability. By the manner of kirigami, the range of synthetic polymer, polyethylene (dark purple region), can be extended to a larger range (mauve region) and thus contain a wide range of biological materials. This makes it mechanically possible to adopt polyethylene as a substitute for biological materials.

local symmetric and anti-symmetric buckling, respectively, while mode Co-occurrence signifies the coexistence of both types of local buckling in different areas of kirigami. These buckling modes persist throughout the post-buckling stage of kirigami and undergo transformations as the geometric parameters vary, highlighting their dependence on geometry. Notably, the buckling modes exhibit a strong correlation with the geometric parameter ℓ_w but are less sensitive to ℓ_{sp} . The stress distribution in finite element simulations for the four typical deformation configurations is depicted in the inset of Fig. 8. It is evident that stress concentrates at the slit tip, while the stress levels elsewhere are relatively low. The overall post-stretching process demonstrates remarkable hardening, representing a significant deformation transformation mechanism from bending and twisting deformation at the slit to stretching deformation. Eventually, as the strain continues to increase, kirigami fails and the material fractures.

Considering the geometric asymmetry, the extended representation of buckling modes in the mechanical response (see Fig. 9) offers valuable insights into the underlying buckling modes during the stretching of kirigami. Based on the four buckling modes observed in geometrically symmetric kirigami, it is evident that local, global, and bilateral modes can be distinguished based on the spatial distribution of local buckling types around the slits. The insets in Fig. 9 illustrate typical deformation configurations associated with different extended buckling modes. This figure enables the prediction of buckling and deformation patterns in different regions of kirigami under the stretching load, providing a solid foundation for target-led pattern parameter design in potential functional applications. These results demonstrate the potential of employing deep learning techniques, rather than complex and time-consuming finite element simulations, to predict buckling and deformation behaviors of kirigami structures during stretching.

To verify the reliability of DL models, experimental examples of kirigami structures are presented in Fig. 10. Four samples were fabricated using a similar experimental approach as described earlier, and displacement field measurements were performed using a T-Cam MR digital camera system. These samples exhibit different buckling modes when subjected to stretching. A comparison of the overall structure's geometric patterns and local details demonstrates the high accuracy of the CNN model classification, as indicated by the classification predictions. Additionally, comparisons between experimental and simulated displacement fields are presented to further support the accuracy of the predictions.

The rational kirigami design described above allows the development of artificial materials with a nonlinear stress-strain response that reproduce a flexible substrate adhered to the surface of biological tissue. For example, Fig. 11 shows two typical kirigami materials whose nonlinear stress-strain curves are very close to those of the human back skin and the articular cartilage. The stress-strain curves rapidly predicted and selected by the RNN model based on the artificial kirigami material match well with the target curves for human back skin and articular cartilage. It showcases the potential application of stress-strain curves predicted by the RNN model in flexible electronics. Two examples of typical kirigami structures are shown, highlighting their suitability and conformability to the human back skin [67] and articular cartilage [68]. Applying such kirigami structures to the surface of the human back enables the detection of body sensors and other specific functions during daily activities without causing any physical discomfort. Furthermore, it is possible to quantitatively tailor the design of kirigami to adapt to different parts of the human body, considering individual variations, thereby satisfying both functionality and comfort requirements. Many biological tissues exhibit anisotropic mechanical properties, which poses a great challenge for the development of artificial kirigami materials with mimetic stress-strain responses. With the proposed RNN model, the response space can be effectively enlarged and compatible with various stress-strain curves, and the ideal stress-strain curves are inversely screened by matching the target biological tissues, thereby identifying the desirable artificial kirigami materials. The green region in Fig. 11 illustrates the capability of kirigami structures to match stress-strain curves, indicating that the developed RNN model can be used to perform kirigami target-led pattern parameter design that accommodates stress-strain curves within this range. Finally, the Ashby plot in Fig. 12 presents Young's modulus and elongation-at-break under stretching. The kirigami operation plays an extraordinary role in the expansion of the Ashby plot. By conducting the kirigami operation on a material, a larger range of regions in the Ashby diagram can be designed and explored with elastic modulus and elongation not greater than that of the material. For instance, the dark purple range representing the PE material can be extended to the light purple range. Noted that this extension is only brought about by the kirigami operation itself, while the deep learning model is built to facilitate fast enumerative prediction and selection in the shallow purple range. This enables the full potential of kirigami to be exploited

and further arbitrary designs of kirigami patterns to be made. The range of performance achievable with kirigami extends beyond that of typical synthetic polymers, encompassing most biological materials. This offers new perspectives for exploring alternative biological materials.

5. Discussion and conclusions

Symmetry, ubiquitously encountered in nature, is a fundamental characteristic of many biological systems, including molecules vital to life, such as amino acids and the saccharide units in starch. Alongside this, nature also demonstrates a predilection for symmetry breaking, manifest as chirality or other forms of discrete structural alterations, which can profoundly influence both structure and functionality. A perfect instance of this is observed in the art of kirigami, where symmetry-breaking designs induce dramatic changes in mechanical responses, making it a promising technique for applications in functional devices, flexible electronics, and biomedical engineering. The mechanics of kirigami, fundamentally, is an intricate interplay between tensile, bending, and torsion energies. However, the science lacks precision tools to harness symmetry breaking in kirigami for enhancing mechanical responses and enabling reverse design.

In this study, we propose a pattern design approach leveraging data-driven techniques based on deep learning (DL). This strategy offers programmable design solutions for the generation of desirable kirigami cutting patterns and their consequent mechanical responses. Inspired by experimental studies and simulation results regarding kirigami cutting patterns, we have developed DL models that encompass a broad design space, incorporating a myriad of unique and accessible constitutive relationships and buckling modes. This data-driven strategy can deliver accurate predictions of intricate nonlinear constitutive relationships and buckling modes by effectively managing large datasets.

Our DL models exploit Convolutional Neural Networks (CNNs) to extract the fundamental features of the kirigami displacement field. The CNN model successfully navigates the challenges posed by image noise, identifying geometric symmetries and symmetry-breaking patterns, and thus effectively classifying buckling patterns. By extracting the stress-strain curves of kirigami structures, Recurrent Neural Networks (RNNs) model, utilizing history-dependent hidden states, efficiently handles sequential data and establishes a connection between geometry and constitutive relationships. Optimal model performance is achieved with the configuration of three GRU layers and 500 neurons in the RNN model. After 200 epochs of iteration, the prediction losses for the training and test sets are remarkably low, further substantiated by low metrics for both sets.

We also note that the local buckling characteristics of kirigami structures are irregular. To account for these, we divide the 3D deformed configurations of geometrically symmetric and geometrically symmetry-breaking kirigami structures into four and eight buckling modes, respectively. These buckling modes show a strong correlation with the geometric parameter ℓ_w and are relatively insensitive to ℓ_{sp} . The robustness of our DL models was validated through tests on four experimental samples and comparisons between experiments and simulations, supporting the accuracy of the predictions.

Finally, our design approach enables the design of a wide variety of kirigami structures to fulfill diverse functional requirements. To demonstrate the utility of our approach, we present two applications: one for human back skin and the other for articular cartilage. Our models suggest that synthetic polymers, when crafted using kirigami techniques, can substitute for biological materials, offering new possibilities in terms of their constitutive relationships and modulus of elasticity. Through our design approach, superior symmetry-breaking pattern candidates with multimodality are obtained to match various movement states and accommodate individual differences in health monitoring and such kirigami with flexibility, comfort, and stretchability can be utilized as mechanically flexible and integrated devices for diagnostics and therapeutics in personalized healthcare. The kirigami

structures studied in this paper are essentially two-dimensional planar structures. The structure undergoes out-of-plane deformation by local buckling during stretching, resulting in three-dimensional structuring. A large number of studies have investigated the optimization of three-dimensional structures [70–73]. In the future, the dimensionality of kirigami structures will continue to be extended to three dimensions in terms of material selection, loading methods, and highly designable performance, leading to advanced kirigami materials that maximize deformation and maximize functionality.

CRediT authorship contribution statement

Yunce Zhang: Writing – original draft, Visualization, Validation, Software, Methodology, Investigation, Formal analysis, Data curation, Conceptualization. **Yafei Wang:** Funding acquisition, Conceptualization, Resources, Supervision, Validation, Visualization, Writing – review & editing. **Qiang Tao:** Investigation, Validation, Visualization. **Yuanpeng Liu:** Funding acquisition, Supervision, Writing – review & editing. **Changguo Wang:** Funding acquisition, Supervision, Writing – review & editing.

Declaration of competing interest

The authors declare that they have no known competing financial interests or personal relationships that could have appeared to influence the work reported in this paper.

Data availability

Data will be made available on request.

Acknowledgments

The authors acknowledge financial supports from National Natural Science Foundation of China, Grant Nos. 12172102, 12002109, 12372097, 12202105, the Fundamental Research Funds for the Central Universities under Grant No. HIT.OCEF.2022013, the Science Foundation of the National Key Laboratory of Science and Technology on Advanced Composites in Special Environments, Grant No. JCKYS2022603C015, Natural Science Foundation of Chongqing, China Nos. cstc2021jcyj-msxmX1035, the China National Postdoctoral Program for Innovative Talents under Grant No. BX20220086, the China Postdoctoral Science Foundation under Grant No. 2022M710751, and Shanghai Post-doctoral Excellence Program under Grant No. 2022732.

Appendix A. Supplementary data

Supplementary material related to this article can be found online at <https://doi.org/10.1016/j.ijmecsci.2024.109331>.

References

- [1] Wang W, Li C, Rodrigue H, Yuan F, Han M-W, Cho M, et al. Kirigami/origami-based soft deployable reflector for optical beam steering. *Adv Funct Mater* 2017;27(7):1604214.
- [2] Tang Y, Lin G, Yang S, Yi YK, Kamien RD, Yin J. Programmable kiri-kirigami metamaterials. *Adv Mater* 2017;29(10):1604262.
- [3] Jang N-S, Kim K-H, Ha S-H, Jung S-H, Lee HM, Kim J-M. Simple approach to high-performance stretchable heaters based on kirigami patterning of conductive paper for wearable thermotherapy applications. *ACS Appl Mater Interfaces* 2017;9(23):19612–21.
- [4] Guan Y-S, Li H, Ren F, Ren S. Kirigami-inspired conducting polymer thermoelectrics from electrostatic recognition driven assembly. *ACS Nano* 2018;12(8):7967–73.
- [5] Li Q, Liu W, Yang C, Rao P, Lv P, Duan H, et al. Kirigami-inspired adhesion with high directional asymmetry. *J Mech Phys Solids* 2022;169:105053.
- [6] Shyu TC, Damasceno PF, Dodd PM, Lamoureux A, Xu L, Shlian M, et al. A kirigami approach to engineering elasticity in nanocomposites through patterned defects. *Nature Mater* 2015;14(8):785–9.

- [7] Isobe M, Okumura K. Initial rigid response and softening transition of highly stretchable kirigami sheet materials. *Sci Rep* 2016;6(1):1–6.
- [8] Wang Y, Wang C. Buckling of ultrastretchable kirigami metastructures for mechanical programmability and energy harvesting. *Int J Solids Struct* 2021;213(2021):93–102.
- [9] Hwang D-G, Bartlett MD. Tunable mechanical metamaterials through hybrid kirigami structures. *Sci Rep* 2018;8(1):3378.
- [10] Taniyama H, Iwase E. Design of rigidity and breaking strain for a kirigami structure with non-uniform deformed regions. *Micromachines* 2019;10(6):395.
- [11] Rafsanjani A, Bertoldi K. Buckling-induced kirigami. *Phys Rev Lett* 2017;118(8):084301.
- [12] Moshe M, Esposito E, Shankar S, Bircan B, Cohen I, Nelson DR, et al. Kirigami mechanics as stress relief by elastic charges. *Phys Rev Lett* 2019;122(4):048001.
- [13] Wang Y, Wang C. Mechanics of strain-limiting wrinkled kirigami for flexible devices: High flexibility, stretchability and compressibility. *Int J Solids Struct* 2022;238:111382.
- [14] Guan Y-S, Zhang Z, Tang Y, Yin J, Ren S. Kirigami-inspired nanoconfined polymer conducting nanosheets with 2000% stretchability. *Adv Mater* 2018;30(20):1706390.
- [15] Moshe M, Esposito E, Shankar S, Bircan B, Cohen I, Nelson DR, et al. Nonlinear mechanics of thin frames. *Phys Rev E* 2019;99(1):013002.
- [16] Xu Z, Jin C, Cabe A, Escobedo D, Gruslova A, Jenney S, et al. Implantable cardiac kirigami-inspired lead-based energy harvester fabricated by enhanced piezoelectric composite film. *Adv Healthc Mater* 2021;10(8):2002100.
- [17] Hu N, Chen D, Wang D, Huang S, Trase I, Grover HM, et al. Stretchable kirigami polyvinylidene difluoride thin films for energy harvesting: design, analysis, and performance. *Phys Rev Appl* 2018;9(2):021002.
- [18] Tang Y, Lin G, Han L, Qiu S, Yang S, Yin J. Design of hierarchically cut hinges for highly stretchable and reconfigurable metamaterials with enhanced strength. *Adv Mater* 2015;27(44):7181–90.
- [19] Won P, Park JJ, Lee T, Ha I, Han S, Choi M, et al. Stretchable and transparent kirigami conductor of nanowire percolation network for electronic skin applications. *Nano Lett* 2019;19(9):6087–96.
- [20] Choi GP, Dudte LH, Mahadevan L. Programming shape using kirigami tessellations. *Nature Mater* 2019;18(9):999–1004.
- [21] Liu Z, Du H, Li J, Lu L, Li Z-Y, Fang NX. Nano-kirigami with giant optical chirality. *Sci Adv* 2018;4(7):eaat4436.
- [22] Ma R, Wu C, Wang ZL, Tsukruk VV. Pop-up conducting large-area biographene kirigami. *ACS Nano* 2018;12(10):9714–20.
- [23] Yu HC, Hao XP, Zhang CW, Zheng SY, Du M, Liang S, et al. Engineering tough metallosupramolecular hydrogel films with kirigami structures for compliant soft electronics. *Small* 2021;17(41):2103836.
- [24] Yang Y, Dias MA, Holmes DP. Multistable kirigami for tunable architected materials. *Phys Rev Mater* 2018;2(11):110601.
- [25] Sadik S, Walker MG, Dias MA. On local kirigami mechanics II: Stretchable creased solutions. *J Mech Phys Solids* 2022;161:104812.
- [26] Sanchez-Lengeling B, Aspuru-Guzik A. Inverse molecular design using machine learning: Generative models for matter engineering. *Science* 2018;361(6400):360–5.
- [27] Cai P, Wang C, Gao H, Chen X. Mechanomaterials: A rational deployment of forces and geometries in programming functional materials. *Adv Mater* 2021;2007977.
- [28] Jiang J, Xiong Y, Zhang Z, Rosen DW. Machine learning integrated design for additive manufacturing. *J Intell Manuf* 2020;1–14.
- [29] Su J-W, Li D, Xie Y, Zhou T, Gao W, Deng H, et al. A machine learning workflow for 4D printing: understand and predict morphing behaviors of printed active structures. *Smart Mater Struct* 2020;30(1):015028.
- [30] Gu GX, Chen C-T, Richmond DJ, Buehler MJ. Bioinspired hierarchical composite design using machine learning: simulation, additive manufacturing, and experiment. *Mater Horiz* 2018;5(5):939–45.
- [31] Ng WL, Goh GL, Goh GD, Sheuan JTJ, Yeong WY. Progress and opportunities for machine learning in materials and processes of additive manufacturing. *Adv Mater* 2024;2310006.
- [32] Xames MD, Torsha FK, Sarwar F. A systematic literature review on recent trends of machine learning applications in additive manufacturing. *J Intell Manuf* 2023;34(6):2529–55.
- [33] Li X, Ning S, Liu Z, Yan Z, Luo C, Zhuang Z. Designing phononic crystal with anticipated band gap through a deep learning based data-driven method. *Comput Methods Appl Mech Engrg* 2020;361:112737.
- [34] Li X, Liu Z, Cui S, Luo C, Li C, Zhuang Z. Predicting the effective mechanical property of heterogeneous materials by image based modeling and deep learning. *Comput Methods Appl Mech Engrg* 2019;347:735–53.
- [35] Wilt JK, Yang C, Gu GX. Accelerating auxetic metamaterial design with deep learning. *Adv Energy Mater* 2020;22(5):1901266.
- [36] Chen C-T, Gu GX. Generative deep neural networks for inverse materials design using backpropagation and active learning. *Adv Sci* 2020;7(5):1902607.
- [37] Gu GX, Chen C-T, Buehler MJ. De novo composite design based on machine learning algorithm. *Extreme Mech Lett* 2018;18:19–28.
- [38] Liu F, Jiang X, Wang X, Wang L. Machine learning-based design and optimization of curved beams for multistable structures and metamaterials. *Extreme Mech Lett* 2020;41:101002.
- [39] Zhao T, Li Y, Zuo L, Zhang K. Machine-learning optimized method for regional control of sound fields. *Extreme Mech Lett* 2021;45:101297.
- [40] Zhang Y, Tao Q, Liu Y, Wang C. Mesh/membrane composite with superior mechanical performance: A deep learning-based design. *Compos Sci Technol* 2022;230:109735.
- [41] Challapalli A, Konkan J, Li G. Inverse machine learning discovered metamaterials with record high recovery stress. *Int J Mech Sci* 2023;244:108029.
- [42] Ha CS, Yao D, Xu Z, Liu C, Liu H, Elkins D, et al. Rapid inverse design of metamaterials based on prescribed mechanical behavior through machine learning. *Nature Commun* 2023;14(1):5765.
- [43] Soni M, Misra S. Machine-learning-assisted design of multiband terahertz metamaterial absorber. *ACS Appl Opt Mater* 2023;1(10):1679–87.
- [44] Liu Z, Wu C. Exploring the 3D architectures of deep material network in data-driven multiscale mechanics. *J Mech Phys Solids* 2019;127:20–46.
- [45] Yang Z, Yu C-H, Guo K, Buehler MJ. End-to-end deep learning method to predict complete strain and stress tensors for complex hierarchical composite microstructures. *J Mech Phys Solids* 2021;104506.
- [46] Sengodan GA. Prediction of two-phase composite microstructure properties through deep learning of reduced dimensional structure-response data. *Composites B* 2021;225:109282.
- [47] Gorji MB, Mozaffar M, Heidenreich JN, Cao J, Mohr D. On the potential of recurrent neural networks for modeling path dependent plasticity. *J Mech Phys Solids* 2020;143:103972.
- [48] Mozaffar M, Bostanabad R, Chen W, Ehmann K, Cao J, Bessa M. Deep learning predicts path-dependent plasticity. *Proc Natl Acad Sci USA* 2019;116(52):26414–20.
- [49] Hanakata PZ, Cubuk ED, Campbell DK, Park HS. Accelerated search and design of stretchable graphene kirigami using machine learning. *Phys Rev Lett* 2018;121(25):255304.
- [50] Rajak P, Wang B, Nomura K-i, Luo Y, Nakano A, Kalia R, et al. Autonomous reinforcement learning agent for stretchable kirigami design of 2D materials. *npj Comput Mater* 2021;7(1):102.
- [51] Alderete NA, Pathak N, Espinosa HD. Machine learning assisted design of shape-programmable 3D kirigami metamaterials. *npj Comput Mater* 2022;8(1):191.
- [52] Cui J, Poblete FR, Zhu Y. Origami/Kirigami-guided morphing of composite sheets. *Adv Funct Mater* 2018;28(44):1802768.
- [53] Babae S, Pajovic S, Rafsanjani A, Shi Y, Bertoldi K, Traverso G. Bioinspired kirigami metasurfaces as assistive shoe grips. *Nat Biomed Eng* 2020;4(8):778–86.
- [54] Zhang Z, Yu Y, Tang Y, Guan Y-S, Hu Y, Yin J, et al. Kirigami-inspired stretchable conjugated electronics. *Adv Electron Mater* 2020;6(1):1900929.
- [55] Guo X, Ni X, Li J, Zhang H, Zhang F, Yu H, et al. Designing mechanical metamaterials with kirigami-inspired, hierarchical constructions for giant positive and negative thermal expansion. *Adv Mater* 2021;33(3):2004919.
- [56] Jin H, Jiao T, Clifton RJ, Kim K-S. Dynamic fracture of a bicontinuously nanotructured copolymer: A deep-learning analysis of big-data-generating experiment. *J Mech Phys Solids* 2022;164:104898.
- [57] Bojarski M, Del Testa D, Dworakowski D, Firner B, Flepp B, Goyal P, et al. End to end learning for self-driving cars. 2016, arXiv preprint arXiv:1604.07316.
- [58] Parkhi O, Vedaldi A, Zisserman A. Deep face recognition. In: BMVC proceedings of the British machine vision conference. British Machine Vision Association; 2015.
- [59] Zhang A, Lipton ZC, Li M, Smola AJ. Dive into deep learning. 2021, arXiv preprint arXiv:2106.11342.
- [60] Young T, Hazarika D, Poria S, Cambria E. Recent trends in deep learning based natural language processing. *IEEE Comput Intell Mag* 2018;13(3):55–75.
- [61] Bengio Y, Simard P, Frasconi P. Learning long-term dependencies with gradient descent is difficult. *IEEE Trans Neural Netw* 1994;5(2):157–66.
- [62] Hochreiter S, Schmidhuber J. Long short-term memory. *Neural Comput* 1997;9(8):1735–80.
- [63] Chung J, Gulcehre C, Cho K, Bengio Y. Empirical evaluation of gated recurrent neural networks on sequence modeling. 2014, arXiv preprint arXiv:1412.3555.
- [64] Keras. Keras API reference. 2021, <https://keras.io/api/>.
- [65] Sharma S, Sharma S, Athaiya A. Activation functions in neural networks. *Towards Data Sci* 2017;6(12):310–6.
- [66] Agarap AF. Deep learning using rectified linear units (relu). 2018, arXiv preprint arXiv:1803.08375.
- [67] Jang K-I, Chung HU, Xu S, Lee CH, Luan H, Jeong J, et al. Soft network composite materials with deterministic and bio-inspired designs. *Nature Commun* 2015;6(1):6566.
- [68] Vazquez KJ, Andreae JT, Henak CR. Cartilage-on-cartilage cyclic loading induces mechanical and structural damage. *J Mech Behav Biomed Mater* 2019;98:262–7.
- [69] Ashby MF. Materials and the environment: eco-informed material choice. Elsevier; 2012.
- [70] Meier T, Li R, Mavrikos S, Blankenship B, Vangelatos Z, Yildizdag ME, et al. Obtaining auxetic and isotropic metamaterials in counterintuitive design spaces: an automated optimization approach and experimental characterization. *npj Comput Mater* 2024;10(1):3.
- [71] Vangelatos Z, Yildizdag ME, Grigoropoulos CP. A designer's challenge: Unraveling the architected structure of deep sea sponges for lattice mechanical metamaterials. *Extreme Mech Lett* 2023;61:102013.

- [72] Sheikh HM, Meier T, Blankenship B, Vangelatos Z, Zhao N, Marcus PS, et al. Systematic design of Cauchy symmetric structures through Bayesian optimization. *Int J Mech Sci* 2022;236:107741.
- [73] Vangelatos Z, Sheikh HM, Marcus PS, Grigoropoulos CP, Lopez VZ, Flamourakis G, et al. Strength through defects: A novel Bayesian approach for the optimization of architected materials. *Sci Adv* 2021;7(41):eabk2218.